Progress In Electromagnetics Research, Vol. 135, 481–513, 2013

AN IMPROVED NONLINEAR CHIRP SCALING ALGORITHM BASED ON CURVED TRAJECTORY IN GEOSYNCHRONOUS SAR

Cheng Hu*, Teng Long, and Ye Tian

Radar Research Lab, Department of Electronic Engineering, Beijing Institute of Technology, Beijing 100081, P. R. China

Abstract—Geosynchronous synthetic aperture radar (GEO SAR) has the characteristics of long aperture time and large imaging area. Therefore, the conventional imaging algorithm in Low Earth Orbit (LEO) SAR loses effect. In this paper, based on curved trajectory model under an ideal acquisition and not considering some acquisition perturbations (atmosphere, orbital deviations), an accurate two-dimensional frequency spectrum is analytically obtained via series reversion principle and high order Taylor expansion. Then, an improved Nonlinear Chirp Scaling (NCS) algorithm is proposed in GEO SAR, which includes novel range migration correction factor, coupling phase compensation factor, NCS factor and azimuth compression function. Finally, the correctness of the proposed NCS algorithm is verified via imaging results of point array targets and area targets.

1. INTRODUCTION

Synthetic Aperture Radar (SAR) has been widely used in many application fields, such as topography mapping, ocean monitoring, etc. However, because of some special application requirements to revisiting time, it is difficult for Low Earth Orbit (LEO) SAR to satisfy the application requirement of short revisit time. Taking WenChuan earthquake for example, the first coarse SAR image (70 m resolution) was obtained after one day of the earthquake, which is not timely to offer useful information for rescuing.

Geosynchronous SAR (GEO SAR) has approximate orbit height as 36500 km, and the orbit repeating period is only one day [1, 2].

Received 26 September 2012, Accepted 7 December 2012, Scheduled 26 December 2012

* Corresponding author: Cheng Hu (hucheng.bit@gmail.com).

Furthermore, one GEO SAR can cover one third of the globe surface, thus the revisiting time is short and less than 24 hour. The maximum revisit time is shown in Fig. 1 with the orbit parameters listed in Table 1. Therefore, the maximum revisit time is less than seven hours for the whole China. In some specific areas, the nearly continuous monitoring can be achieved. For these reasons, GEO SAR can play an important role in future disaster monitoring and alarm [3–5], as well as some other application fields such as land measurement, soil moisture monitoring, atmosphere vapor map, micro-deformation monitoring, etc.

With its fine temporal resolution and large coverage, Geosynchronous SAR (GEO SAR) was firstly presented in [1, 2], in which the orbit height was close to 36500 km. In this paper, the whole United States can be imaged in about 3 h of segmented operation at 100-m resolution with 4-azimuth-look averaging from a 50 degrees inclined circular orbit. In addition, one GEO SAR can provide daily coverage for approximately 1/3 of the globe [3]; disaster areas can be monitored in the range of 1.5–2.5 hours per day [3]. Therefore, the GEO SAR has a lot of advantages in disaster prediction, disaster management, ocean applications, earth dynamics and so on [6, 7].

Further studies were presented in 2001, when Jet Propulsion Laboratory (JPL) proposed a GEO SAR system concept with the orbital inclination angle of 50°–65°. In 2003, JPL launched the Global Earthquake Satellite System (GESS) plan and pointed out that the deployment of GEO SAR satellite would be a massive undertaking requiring major technological challenges to be overcome. However, it might be considered as a mission for the next decade [7]. The work of

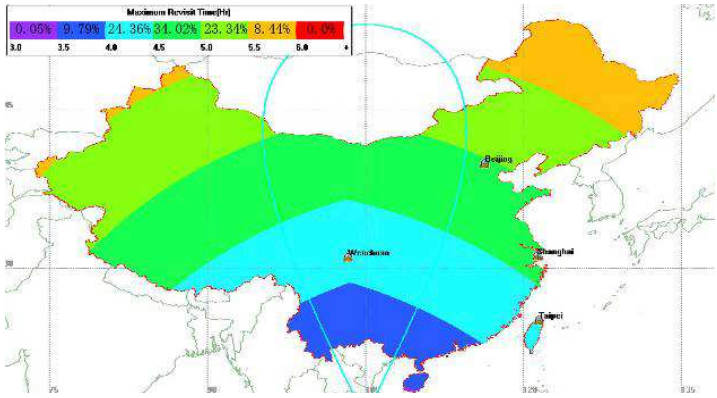

Figure 1. Maximum revisit time for single GEO SAR.

Politecnico di Milano on small inclination GEO missions is focused on parasitic Bistatic SAR [8, 9]. The GEO satellite is located into a nearly geostationary orbit, using TV broadcasting satellite as illuminators of opportunity, and the received is stationary on the ground or runs in geosynchronous orbit. From 2008 till now, the China Aerospace Science and Technology Corporation (CASC) launched the research of the GEO SAR system conception, parameters design and so on. Especially in 2011, the Chinese government planned to launch a GEO SAR satellite in the next several years for monitoring of emergency natural disasters.

At present, the related literature about GEO SAR is mainly focused on the system parameters design, ionosphere and atmosphere effect, and application requirements [10, 11]. Hobbs et al. firstly studied the impacts of troposphere and ionosphere on GEO SAR imaging [12–15]. For the signal characteristic and imaging algorithms, the related literature is mainly concentrated on the modification of conventional SAR imaging algorithms in GEO SAR, such as modified SPECtrum ANalysis (SPECAN) algorithm, modified Secondary Range Compression (SRC) algorithm, modified Polar Format Algorithm (PFA) and so on [16–22]. However, there is no special imaging algorithm for GEO SAR curved trajectory (not circular trajectory). Circular SAR (CSAR) was proposed in spotlight mode in the 1990s [23], and various imaging techniques are discussed in [24–27], such as confocal [24] or back-projection (BP) [25] algorithms or wavefront reconstruction theory-based method with Green's function [26, 27], but these algorithms have the disadvantage of computational inefficiency and cannot be used in GEO SAR because of circular motion trajectory.

Beside the effect of curved trajectory, the large orbit height will result in large observation swath (single beam 400 km–500 km), and the earth rotation will result in un-ignorable squint angle. Therefore, target slant range history has large spatial variance. The GEO SAR imaging processing must consider the spatial variance of slant range history and the compensation of two-dimensional coupling phase in frequency domain under long synthetic aperture time [28–31]. Nonlinear Chirp Scaling (NCS) algorithm, widely used in squint imaging processing of airborne SAR and LEO SAR [32–34], considers the scene spatial variance and compensates the two-dimensional coupling phase. At present, the NCS algorithm is based on the equivalent linear trajectory model. Therefore, the derived compensation factor can't be directly used in GEO SAR, and even the NCS algorithm loses effect in GEO SAR special position such as Apogee. This paper aims to the problems of curved trajectory and

large scene focusing in GEO SAR. The improved NCS algorithm for GEO SAR is analytically derived based on curved trajectory model and the novel compensation factor of spatial variance and high order coupling phase are obtained. Furthermore, the imaging results of NCS algorithm are verified via simulation data.

The system geometric structure and slant range model are analyzed in second section, the analytical frequency spectrum is obtained in third section, the improved NCS algorithm is derived in forth section and the simulation results and performance evaluation are shown in fifth section. Finally, the conclusion is drawn.

2. GEOMETRIC STRUCTURE AND SLANT RANGE MODEL

2.1. GEO SAR Geometric Structure

In low earth orbit, the satellite trajectory can be approximated to a straight line, as shown in Fig. 2. According to the geometric relations in Fig. 2, the slant range history (R_n) between the satellite and target can be expressed as

$$R_n = \sqrt{R_c^2 + (v \cdot t_a)^2 - 2 \cdot R_c \cdot (v \cdot t_a) \cdot \sin\theta} \tag{1}$$

where R_c is the slant range when the beam center arrives at the point target; v is the satellite velocity; t_a is the azimuth-time; θ is the squint angle. Formula (1) is known as the linear trajectory model.

Under the condition of typical parameters $\theta = 0$, $v = 7062\,\mathrm{m/s}$, $R_{\min} = 800\,\mathrm{km}$, the result of the slant history in LEO SAR is shown in Fig. 3. Obviously, the slant range undergoes a course from far range

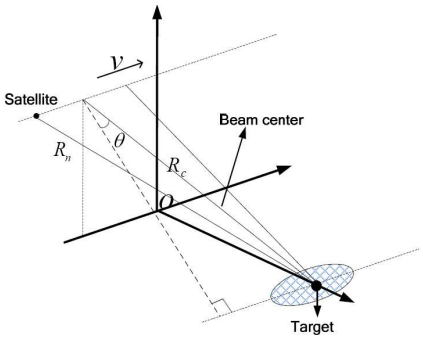

Figure 2. General geometric structure of LEO SAR.

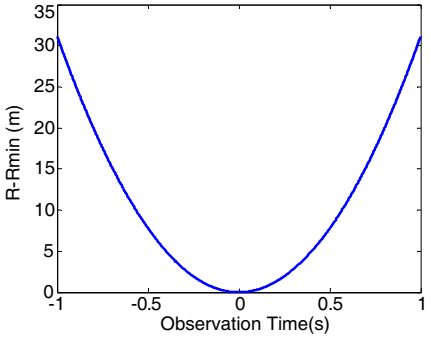

Figure 3. Slant range history in LEO SAR.

to near range, and then to far range again, which is called the "far-near-far" model. However, the situation in GEO SAR is not always the same as that in LEO SAR due to the rotation of the earth and elliptical orbit effect. In order to illustrate this problem, the orbital parameters listed in Table 1 are selected for simulation. These parameters are designed to basically cover the whole China. The nadir-point track and geometrical structure of GEO SAR are plotted in Fig. 4 and Fig. 5.

In LEO SAR, because of the short synthetic aperture considered, the synthetic aperture can be approximated as a linear trajectory, shown in dotted frame in Fig. 5. However, in order to achieve proper resolution in GEO SAR, the synthetic aperture time has to be increased up to hundreds of seconds. Therefore, the conventional linear trajectory model will not be valid resulting in large error.

According to the parameters listed in Table 1, when the GEO SAR satellite passes the perigee, the slant history is similar to the case in LEO SAR. On the other hand, the slant range history is opposite to

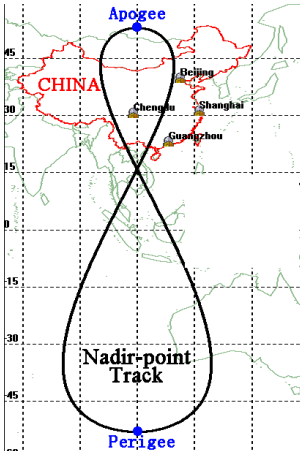

Figure 4. Nadir-point track of GEO SAR.

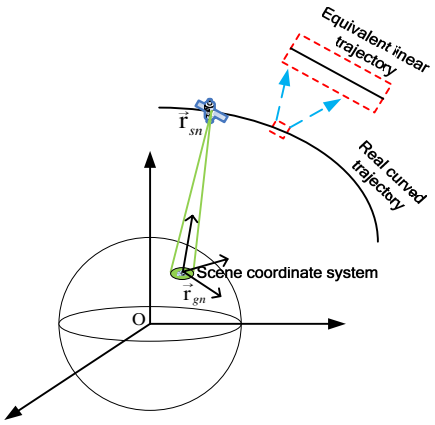

Figure 5. Geometric structure of GEO SAR.

Table 1. GEO SAR orbit parameters.

Parameters	Value	Unit
Semi Major Axis	42164.17	km
Inclination	53	degrees
Argument of Perigee	270	degrees
Eccentricity	0.07	

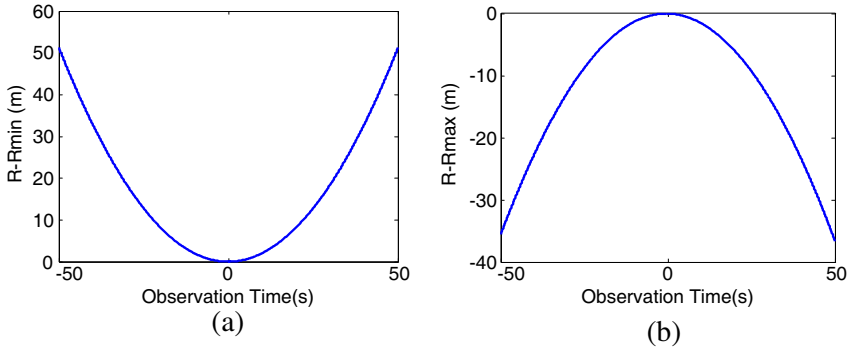

Figure 6. Actual slant range histories in GEO SAR. (a) Synthetic aperture center in Perigee. (b) Synthetic aperture center in Apogee.

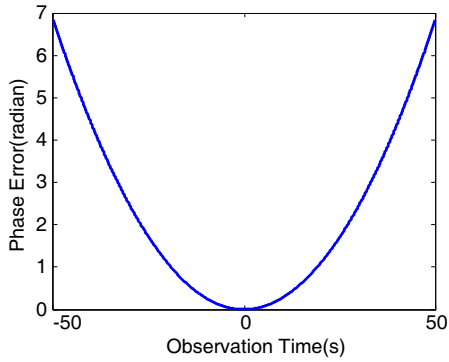

Figure 7. Phase error caused by the linear trajectory model.

the case in LEO SAR when the GEO SAR satellite passes the apogee. In Figs. 6(b), the slant range undergoes a course from near range to far range, then to near range again, which is called the "near-far-near" model.

Therefore, it is difficult to fit the slant range via the linear trajectory when the satellite passes the apogee, or else the velocity and squint angle will be complex numbers. Furthermore, although the slant range in Perigee can be fitted by the linear trajectory, there will be a great fitting error, as shown in Fig. 7. The point target is set at (5 km, 0 km), carrier frequency is 3.2 GHz (wavelength is 0.09375 m). It can be found that the error is as high as 6.8 radians, which is far beyond the limit of 0.78 ($\pi/4$) radians [35]. Thus, the focusing area is also strictly limited by the linear trajectory model at perigee.

2.2. Slant Range Model in GEO SAR

Traditional imaging algorithms, such as Range Doppler (RD) algorithm, Chirp Scaling (CS) algorithm, Nonlinear Chirp Scaling (NCS) algorithm are based on the linear trajectory model or the Fresnel approximation [36–40], but the error of linear trajectory model is considerable in GEO SAR for the long synthetic aperture time. In literature [29], a curved trajectory model is put forward to fit the real slant range history, and an improved SPECAN algorithm is proposed to focus one target point accurately. However, the curved trajectory in the literature is based on the scene central point, and different target positions will appear on different errors when focusing large scenes. Thus, it is necessary to further update curved trajectory model for large scenes focusing.

The curved trajectory model in literature [29] is high order Taylor expansion, which can be shown as

$$R_n = R + k_1 \cdot t_a + k_2 \cdot t_a^2 + k_3 \cdot t_a^3 + k_4 \cdot t_a^4 + \ldots \tag{2}$$

The coefficient of Taylor expansion in Equation (2) is based on scene central point. In order to express the real slant range of any target position in large scene, we further use Taylor expansion on Equation (2) along range direction, we have

$$k_1 = k_{10} + \dot{k}_1 \cdot (R - R_0) \tag{3}$$

$$k_2 = k_{20} + \dot{k}_2 \cdot (R - R_0) \tag{4}$$

$$k_3 = k_{30} + \dot{k}_3 \cdot (R - R_0) \tag{5}$$

$$k_4 = k_{40} + \dot{k}_4 \cdot (R - R_0) \tag{6}$$

where

$$k_{10} = \vec{\mathbf{v}}_{s0} \cdot (\vec{\mathbf{r}}_{s0} - \vec{\mathbf{r}}_{g0})^T / \|\vec{\mathbf{r}}_{s0} - \vec{\mathbf{r}}_{g0}\| \tag{7}$$

$$k_{20} = \frac{\vec{\mathbf{a}}_{s0} \cdot (\vec{\mathbf{r}}_{s0} - \vec{\mathbf{r}}_{g0})^T + \|\vec{\mathbf{v}}_{s0}\|^2}{2 \cdot \|\vec{\mathbf{r}}_{s0} - \vec{\mathbf{r}}_{g0}\|} - \frac{\left[\vec{\mathbf{v}}_{s0} \cdot (\vec{\mathbf{r}}_{s0} - \vec{\mathbf{r}}_{g0})^T\right]^2}{2 \cdot \|\vec{\mathbf{r}}_{s0} - \vec{\mathbf{r}}_{g0}\|^3} \tag{8}$$

$$k_{30} = \frac{\vec{\mathbf{b}}_{s0} \cdot (\vec{\mathbf{r}}_{s0} - \vec{\mathbf{r}}_{g0})^T + 3 \cdot \vec{\mathbf{a}}_{s0} \cdot \vec{\mathbf{v}}_{s0}^T}{6 \cdot \|\vec{\mathbf{r}}_{s0} - \vec{\mathbf{r}}_{g0}\|} + \frac{\left[\vec{\mathbf{v}}_{s0} \cdot (\vec{\mathbf{r}}_{s0} - \vec{\mathbf{r}}_{g0})^T\right]^3}{2 \cdot \|\vec{\mathbf{r}}_{s0} - \vec{\mathbf{r}}_{g0}\|^5} - \frac{\vec{\mathbf{v}}_{s0} \cdot (\vec{\mathbf{r}}_{s0} - \vec{\mathbf{r}}_{g0})^T \cdot \vec{\mathbf{a}}_{s0} \cdot (\vec{\mathbf{r}}_{s0} - \vec{\mathbf{r}}_{g0})^T}{2 \cdot \|\vec{\mathbf{r}}_{s0} - \vec{\mathbf{r}}_{g0}\|^3} - \frac{\vec{\mathbf{v}}_{s0} \cdot (\vec{\mathbf{r}}_{s0} - \vec{\mathbf{r}}_{g0})^T \cdot \|\vec{\mathbf{v}}_{s0}\|^2}{2 \cdot \|\vec{\mathbf{r}}_{s0} - \vec{\mathbf{r}}_{g0}\|^3} \tag{9}$$

$$k_{40} = \frac{\vec{\mathbf{d}}_{s0} \cdot (\vec{\mathbf{r}}_{s0} - \vec{\mathbf{r}}_{g0})^T + 4 \cdot \vec{\mathbf{b}}_{s0} \cdot \vec{\mathbf{v}}_{s0}^T}{24 \cdot \|\vec{\mathbf{r}}_{s0} - \vec{\mathbf{r}}_{g0}\|} + \frac{\|\vec{\mathbf{a}}_{s0}\|^2}{8 \cdot \|\vec{\mathbf{r}}_{s0} - \vec{\mathbf{r}}_{g0}\|} - \frac{k_2^2 + 2 \cdot k_1 \cdot k_3}{2 \cdot \|\vec{\mathbf{r}}_{s0} - \vec{\mathbf{r}}_{g0}\|} \tag{10}$$

$$\dot{k}_1 = \frac{v_{s0x}}{r_{s0x}} - \frac{\vec{\mathbf{v}}_{s0} \cdot (\vec{\mathbf{r}}_{s0} - \vec{\mathbf{r}}_{g0})^T}{R_0^2} \tag{11}$$

$$\begin{aligned}\dot{k}_2 = & \frac{a_{s0x} \cdot R_0^2 - r_{s0x} \cdot \left(\vec{\mathbf{a}}_{s0} \cdot (\vec{\mathbf{r}}_{s0} - \vec{\mathbf{r}}_{g0})^T + \|\vec{\mathbf{v}}_{s0}\|^2\right)}{2 \cdot R_0^2 \cdot r_{s0x}} \\ & - \frac{v_{s0x} \cdot \vec{\mathbf{v}}_{s0} \cdot (\vec{\mathbf{r}}_{s0} - \vec{\mathbf{r}}_{g0})^T}{R_0^2 \cdot r_{s0x}} + \frac{3 \cdot \vec{\mathbf{v}}_{s0} \cdot (\vec{\mathbf{r}}_{s0} - \vec{\mathbf{r}}_{g0})^T}{2 \cdot R_0^4}\end{aligned} \tag{12}$$

$$\begin{aligned}\dot{k}_3 = & \frac{b_{s0x} \cdot R_0^2 - r_{s0x} \cdot \left[\vec{\mathbf{b}}_{s0} \cdot (\vec{\mathbf{r}}_{s0} - \vec{\mathbf{r}}_{g0})^T + 3 \cdot \vec{\mathbf{a}}_{s0} \cdot \vec{\mathbf{v}}_{s0}^T\right]}{6 \cdot R_0^2 \cdot r_{s0x}} \\ & + \frac{3 \cdot v_{s0x} \cdot \left[\vec{\mathbf{v}}_{s0} \cdot (\vec{\mathbf{r}}_{s0} - \vec{\mathbf{r}}_{g0})^T\right]^2 - 5 \cdot r_{s0x} \cdot \left[\vec{\mathbf{v}}_{s0} \cdot (\vec{\mathbf{r}}_{s0} - \vec{\mathbf{r}}_{g0})^T\right]^3}{2 \cdot R_0^6 \cdot r_{s0x}} \\ & - \frac{v_{s0x} \cdot \vec{\mathbf{a}}_{s0} \cdot (\vec{\mathbf{r}}_{s0} - \vec{\mathbf{r}}_{g0})^T + a_{s0x} \cdot \vec{\mathbf{v}}_{s0} \cdot (\vec{\mathbf{r}}_{s0} - \vec{\mathbf{r}}_{g0})^T}{2 \cdot R_0^2 \cdot r_{s0x}} \\ & + \frac{3 \cdot \vec{\mathbf{v}}_{s0} \cdot (\vec{\mathbf{r}}_{s0} - \vec{\mathbf{r}}_{g0})^T \cdot \vec{\mathbf{a}}_{s0} \cdot (\vec{\mathbf{r}}_{s0} - \vec{\mathbf{r}}_{g0})^T}{2 \cdot R_0^4} \\ & - \frac{v_{s0x} \cdot \|\vec{\mathbf{v}}_{s0}\|^2}{2 \cdot R_0^2 \cdot r_{s0x}} + \frac{3 \cdot \vec{\mathbf{v}}_{s0} \cdot (\vec{\mathbf{r}}_{s0} - \vec{\mathbf{r}}_{g0})^T \cdot \|\vec{\mathbf{v}}_{s0}\|^2}{2 \cdot R_0^4}\end{aligned} \tag{13}$$

$$\begin{aligned}\dot{k}_4 = & \frac{d_{s0x} \cdot R_0^2 - r_{s0x} \cdot \left[\vec{\mathbf{d}}_{s0} \cdot (\vec{\mathbf{r}}_{s0} - \vec{\mathbf{r}}_{g0})^T + 4 \cdot \vec{\mathbf{b}}_{s0} \cdot \vec{\mathbf{v}}_{s0}^T\right]}{24 \cdot R_0^2 \cdot r_{s0x}} - \frac{\|\vec{\mathbf{a}}_{s0}\|^2}{8 \cdot R_0^2} \\ & + \frac{k_{20} \cdot \dot{k}_2 + k_{30} \cdot \dot{k}_1 + k_{10} \cdot \dot{k}_3}{r_{s0x}} + \frac{k_{20}^2 + 2 \cdot k_{10} \cdot k_{30}}{2 \cdot R_0^2}\end{aligned} \tag{14}$$

The most relevant parameters and vectors used in Equations (7)–(14) are shown in Fig. 8. The satellite moves along the elliptical orbit with an angular velocity $\overrightarrow{\boldsymbol{\omega}_{\mathbf{s}}}$, the direction of which is along the normal of the orbit plane. The earth center O is one of the focuses of elliptical orbit and is also the origin of earth inertial coordinate system $OXYZ$. In the $OXYZ$, the earth rotates with the angular velocity $\overrightarrow{\boldsymbol{\omega}_{\mathbf{e}}} = [0, 0, \boldsymbol{\omega}_{\mathbf{e}}]$, the direction of which is along the normal of the earth's equatorial plane.

As shown in Fig. 8, $\vec{\mathbf{r}}_{s0}$, $\vec{\mathbf{r}}_{g0}$ and $\vec{\mathbf{v}}_{s0}$ are the satellite position vector, scene center position vector and satellite velocity vector at aperture center moment in $OXYZ$ respectively. $\mathbf{R_0}$ is the distance from the satellite to reference point at aperture center moment.

$\vec{\mathbf{a}}_{s0}$, $\vec{\mathbf{b}}_{s0}$ and $\vec{\mathbf{d}}_{s0}$ are the acceleration velocity vector, the derivate of $\vec{\mathbf{a}}_{s0}$ and the derivate of $\vec{\mathbf{b}}_{s0}$ at aperture center moment respectively.

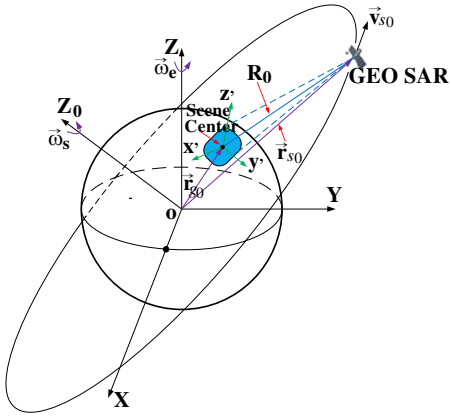

Figure 8. Relevant parameters and vectors in GEO SAR.

r_{s0x}, v_{s0x}, a_{s0x}, b_{s0x} and d_{s0x} are the components of $\vec{\mathbf{r}}_{s0}$, $\vec{\mathbf{v}}_{s0}$, $\vec{\mathbf{a}}_{s0}$, $\vec{\mathbf{b}}_{s0}$ and $\vec{\mathbf{d}}_{s0}$ in scene coordinate system along range direction respectively.

3. TWO-DIMENSIONAL ANALYTICAL FREQUENCY SPECTRUM BASED ON CURVED TRAJECTORY

The Nonlinear Chirp Scaling (NCS) algorithm starts from two-dimension frequency domain, based on the linear trajectory model, the precise two-dimension frequency spectrum can be obtained through principle of stationary phase (POSP) in range and azimuth. However the slant range model in this paper is based on curved trajectory, so it is difficult to obtain stationary phase point in azimuth direction through POSP. Anyway, series reversion is a good method to obtain the stationary phase point for curved trajectory model [41, 42]. Solving the two-dimension frequency spectrum is not the key-point in this paper (the detail in Appendix A). We give the expression of two-dimension frequency spectrum directly as

$$S(f_r, f_a) = \mathbf{u}_r\left(\frac{f_r}{K_r}\right)\cdot \mathbf{u}_a\left[f_a + \frac{2\cdot k_1}{c}\cdot(f_r + f_c)\right]\cdot \exp\left(-\mathbf{j}\cdot\pi\cdot\frac{f_r^2}{K_r}\right)$$
$$\exp\left\{\mathbf{j}\cdot 2\cdot\pi\cdot\left[\begin{array}{l} -\frac{2\cdot(f_r+f_c)}{c}\cdot R \\ +\frac{1}{4\cdot k_2}\cdot\left(\frac{c}{2\cdot(f_r+f_c)}\right)\cdot\left(f_a+\frac{2\cdot k_1}{c}\cdot(f_r+f_c)\right)^2 \\ +\frac{k_3}{8\cdot k_2^3}\cdot\left(\frac{c}{2\cdot(f_r+f_c)}\right)^2\cdot\left(f_a+\frac{2\cdot k_1}{c}\cdot(f_r+f_c)\right)^3 \\ +\frac{9\cdot k_3^2-4\cdot k_2\cdot k_4}{64\cdot k_2^5}\cdot\left(\frac{c}{2\cdot(f_r+f_c)}\right)^3\cdot\left(f_a+\frac{2\cdot k_1}{c}\cdot(f_r+f_c)\right)^4 \end{array}\right]\right\} \quad (15)$$

where f_r and f_a are the range frequency and azimuth frequency, $u_r(\cdot)$ and $u_a(\cdot)$ are the envelope in range direction and azimuth direction, K_r is Frequency-Modulated (FM) rate, c is light speed.

According to (15), as we can see that there is serious coupling between range direction and azimuth direction in two-dimension frequency spectrum, thus it is necessary to decouple and compensate spatial variation if we want to focus large scene. After derivation and simplification to (15), we can obtain two-dimension frequency spectrum as

$$\begin{aligned} S(f_r, f_a) \;=\; & u_r\left(\frac{f_r}{K_r}\right) \cdot u_a\left[f_a + \frac{2k_1}{c}(f_r + f_c)\right] \\ & \cdot \underbrace{\exp\left[\mathbf{j}\cdot 2\cdot\pi\cdot\phi_{az}(f_a, R)\right]}_{\text{azimuth modulation term}} \cdot \underbrace{\exp\left[\mathbf{j}\cdot 2\cdot\pi\cdot\phi_{RP}(R)\right]}_{\text{residual phase term}} \\ & \cdot \underbrace{\exp\left[-\mathbf{j}\cdot 2\cdot\pi\cdot b(f_a, f_r)\right]}_{\substack{\text{a part of migration phase at the} \\ \text{reference point (special term)}}} \cdot \underbrace{\exp\left[-\mathbf{j}\cdot\frac{4\cdot\pi\cdot R}{c\cdot M(f_a)}\cdot f_r\right]}_{\substack{\text{range cell migration term} \\ \text{(including spatial variance)}}} \\ & \cdot \underbrace{\exp\left[-\mathbf{j}\cdot\pi\cdot\frac{f_r^2}{K_s(f_a, R)}\right]}_{\substack{\text{range modulation term} \\ \text{(new range modulation factor)}}} \cdot \underbrace{\exp\left[\mathbf{j}\cdot\phi_3(f_a, R)\cdot f_r^3\right]}_{\substack{\text{two-dimensional coupling} \\ \text{phase term}}} \end{aligned} \tag{16}$$

In the following, we will give the detailed expression of each phase term in Equation (16).

(1) $\phi_{az}(f_a, R)$ is the azimuth modulation function and can be expressed as

$$\begin{aligned} \phi_{az}(f_a, R) = & \left[\frac{k_1}{2\cdot k_2} + \frac{3\cdot k_1^2\cdot k_3}{8\cdot k_2^3} + \frac{k_1^3\cdot\left(9\cdot k_3^2 - 4\cdot k_2\cdot k_4\right)}{16\cdot k_2^5}\right]\cdot f_a \\ & + \left[\frac{\lambda}{8\cdot k_2} + \frac{3\cdot\lambda\cdot k_1\cdot k_3}{16\cdot k_2^3} + \frac{3\cdot\lambda\cdot k_1^2\cdot\left(9\cdot k_3^2 - 4\cdot k_2\cdot k_4\right)}{64\cdot k_2^5}\right]\cdot f_a^2 \\ & + \left[\frac{\lambda^2\cdot k_3}{32\cdot k_2^3} + \frac{\lambda\cdot k_1\cdot\left(9\cdot k_3^2 - 4\cdot k_2\cdot k_4\right)}{64\cdot k_2^5}\right]\cdot f_a^3 + \frac{\lambda^3\cdot\left(9\cdot k_3^2 - 4\cdot k_2\cdot k_4\right)}{512\cdot k_2^5}\cdot f_a^4 \end{aligned} \tag{17}$$

$\phi_{az}(f_a, R)$ is azimuth compression function and only related to azimuth Doppler frequency and target location, rather than range frequency. Thus, it can be compensated in range-doppler domain. We should note that the azimuth compression function depends on the linear term, quadratic term, cubic term and quartic term of azimuth doppler frequency because of curved trajectory, it is totally different from

the azimuth compression function in conventional NCS algorithm. In addition, the coefficients of k_2 and k_4 in (17) will be updated with (4) and (6) along the range direction in order to focus large scene.

2) $\phi_{RP}(R)$ is the residual phase after Taylor expansion and can be expressed as

$$\phi_{RP}(R) = \frac{k_1^2}{2\cdot\lambda\cdot k_2} + \frac{k_1^3\cdot k_3}{4\cdot\lambda\cdot k_2^3} + \frac{k_1^4\cdot\left(9\cdot k_3^2 - 4\cdot k_2\cdot k_4\right)}{32\cdot\lambda\cdot k_2^5} - \frac{2\cdot R}{\lambda} \quad (18)$$

Equation (18) has nothing to do with azimuth Doppler frequency and range frequency, but has relation with target location along range direction, thus it can be compensated in range-doppler domain. Equation (18) includes two parts, the first three phase terms are introduced by spatial variation, and the fourth phase term is the slant range information which connects with target location and can be used in GEO SAR interferometry and GEO SAR differential interferometry.

3) $b(f_a, f_r)$ is a part of the migration phase at the reference point, this term does not exist in conventional CS and NCS algorithms based on linear trajectory model. It is unique term in NCS algorithm based on curved trajectory and must be compensated. Because there is without spatial variance to this term, it can be compensated in two-dimension frequency domain.

$$\begin{aligned} b(f_a, f_r) = &-\left[\frac{k_{10}^2}{2\cdot k_{20}\cdot c} + \frac{k_{10}^3\cdot k_{30}}{4\cdot k_{20}^3\cdot c} + \frac{k_{10}\cdot\left(9\cdot k_{30}^2 - 4\cdot k_{20}\cdot k_{40}\right)}{32\cdot c\cdot k_{20}^5}\right]\cdot f_r \\ &+\left[\frac{\lambda}{8\cdot k_{20}\cdot f_c} + \frac{3\cdot\lambda\cdot k_{10}\cdot k_{30}}{16\cdot k_{20}^3\cdot f_c} + \frac{3\cdot\lambda\cdot k_{10}^2\cdot\left(9\cdot k_{30}^2 - 4\cdot k_{20}\cdot k_{40}\right)}{64\cdot f_c\cdot k_{20}^5}\right]\cdot f_a^2\cdot f_r \\ &+\left[\frac{\lambda^2\cdot k_{30}}{16\cdot k_{20}^3\cdot f_c} + \frac{\lambda^2\cdot k_{10}\cdot\left(9\cdot k_{30}^2 - 4\cdot k_{20}\cdot k_{40}\right)}{32\cdot f_c\cdot k_{20}^5}\right]\cdot f_a^3\cdot f_r \\ &+\frac{3\cdot\lambda^2\cdot\left(9\cdot k_{30}^2 - 4\cdot k_{20}\cdot k_{40}\right)}{512\cdot f_c\cdot k_{20}^5} f_a^4\cdot f_r + \left(\frac{2\cdot R_0}{c} - \dot{B}_1\cdot R_0\right)\cdot f_r \end{aligned} \quad (19)$$

where

$$\begin{aligned} \dot{B}_1 = &-\frac{2\cdot k_{10}\cdot k_{20}\cdot\dot{k}_1 - k_{10}^2\cdot\dot{k}_2}{2\cdot c\cdot k_{20}^2} \\ &-\frac{\left(3\cdot k_{10}^2\cdot k_{30}\cdot\dot{k}_1 + k_{10}^3\cdot\dot{k}_3\right)\cdot k_{20} - 3\cdot k_{10}^3\cdot k_{30}\cdot\dot{k}_2}{4\cdot c\cdot k_{20}^4} - \frac{A_3\cdot\dot{k}_1 - k_{10}\cdot\dot{A}_3}{32\cdot c} \\ &+\left\{-\frac{\lambda\cdot\dot{k}_2}{8\cdot f_c\cdot k_{20}^2} + \frac{3\cdot\lambda\cdot\left[\left(k_{10}\cdot\dot{k}_3 + k_{30}\cdot\dot{k}_1\right)\cdot k_{20} - 3\cdot k_{10}\cdot k_{30}\cdot\dot{k}_2\right]}{16\cdot f_c\cdot k_{20}^4}\right. \end{aligned}$$

$$+\frac{3\cdot\lambda\cdot\left(2\cdot k_{10}\cdot A_3\cdot\dot{k}_1-k_{10}^2\cdot\dot{A}_3\right)}{64\cdot f_c}\Bigg\}\cdot f_a^2$$
$$+\left[\frac{\lambda^2\cdot\left(k_{20}\cdot\dot{k}_3-3\cdot k_{30}\cdot\dot{k}_2\right)}{16\cdot f_c\cdot k_{20}^4}+\frac{\lambda^2\cdot\left(A_3\cdot\dot{k}_1-k_{10}\cdot\dot{A}_3\right)}{32\cdot f_c}\right]\cdot f_a^3$$
$$+\frac{3\cdot\lambda^2\cdot\dot{A}_3}{512\cdot f_c}\cdot f_a^4+\frac{2}{c} \tag{20}$$

$$A_3=\frac{9\cdot k_{30}^2-4\cdot k_{20}\cdot k_{40}}{k_{20}^5} \tag{21}$$

$$\dot{A}_3=\frac{\begin{array}{c}\left[18\cdot k_{30}\cdot\dot{k}_3-4\cdot\left(k_{20}\cdot\dot{k}_4+k_{40}\cdot\dot{k}_2\right)\right]\\ \cdot k_{20}-5\cdot\left(9\cdot k_{30}^2-4\cdot k_{20}\cdot k_{40}\right)\cdot\dot{k}_2\end{array}}{k_{20}^6} \tag{22}$$

4) In Equation (16), the fourth term is range cell migration term and is different (spatial variant) for different target locations along range direction. The spatial variance is adjusted by multiplying a chirp signal in range-doppler domain in CS algorithm. It is also needed in NCS algorithm. $M(f_a)$ is referred as migration factor and can be expressed as

$$M(f_a)=\frac{2}{\dot{B}_1\cdot c} \tag{23}$$

where the expression of $\dot{B}_1$ is shown in (20). The compensation of range cell migration will be presented in Section 4.2 and Section 4.3 in detail.

5) In Equation (16), the fifth term is frequency modulation function in range direction, where $K_s(f_a,R)$ is new Frequency-Modulated (FM) factor in range direction because of the coupling of range frequency and azimuth frequency, and $K_s(f_a,R)$ can be expressed as

$$\frac{1}{K_s(f_a,R)}=-\left[\frac{\lambda}{4\cdot k_2\cdot f_c^2}+\frac{3\cdot\lambda\cdot k_1\cdot k_3}{8\cdot k_2^3\cdot f_c^2}+\frac{3\cdot\lambda\cdot k_1^2\cdot\left(9\cdot k_3^2-4\cdot k_2\cdot k_4\right)}{32\cdot k_2^5\cdot f_c^2}\right]\cdot f_a^2$$
$$-\left[\frac{3\cdot\lambda^2\cdot k_3}{16\cdot k_2^3\cdot f_c^2}+\frac{3\cdot\lambda^2\cdot k_1\cdot\left(9\cdot k_3^2-4\cdot k_2\cdot k_4\right)}{32\cdot k_2^5\cdot f_c^2}\right]\cdot f_a^3$$
$$-\frac{3\cdot\lambda^3\cdot\left(9\cdot k_3^2-4\cdot k_2\cdot k_4\right)}{128\cdot k_2^5\cdot f_c^2}\cdot f_a^4+\frac{1}{K_r} \tag{24}$$

$K_s(f_a, R)$ also has spatial variance, and the spatial variance is generally ignored in CS algorithm. However it is a part of spatial variance modulation in NCS algorithm based on curved trajectory model, in order to compensate spatial variance of $K_s(f_a, R)$, it can be re-expressed as

$$K_s(f_a, R) = K_s(f_a, R_0) + \Delta k_s(f_a) \cdot [\tau(f_a, R) - \tau(f_a, R_0)] \tag{25}$$

where

$$\begin{aligned}\frac{1}{K_s(f_a, R_0)} = &-\left[\frac{\lambda}{4 \cdot k_{20} \cdot f_c^2} + \frac{3 \cdot \lambda \cdot k_{10} \cdot k_{30}}{8 \cdot k_{20}^3 \cdot f_c^2}\right. \\ &\left.+\frac{3 \cdot \lambda \cdot k_{10}^2 \cdot \left(9 \cdot k_{30}^2 - 4 \cdot k_{20} \cdot k_{40}\right)}{32 \cdot k_{20}^5 \cdot f_c^2}\right] \cdot f_a^2 \\ &-\left[\frac{3 \cdot \lambda^2 \cdot k_{30}}{16 \cdot k_{20}^3 \cdot f_c^2} + \frac{3 \cdot \lambda^2 \cdot k_{10} \cdot \left(9 \cdot k_{30}^2 - 4 \cdot k_{20} \cdot k_{40}\right)}{32 \cdot k_{20}^5 \cdot f_c^2}\right] \cdot f_a^3 \\ &-\frac{3 \cdot \lambda^3 \cdot \left(9 \cdot k_{30}^2 - 4 \cdot k_{20} \cdot k_{40}\right)}{128 \cdot k_{20}^5 \cdot f_c^2} \cdot f_a^4 + \frac{1}{K_r}\end{aligned} \tag{26}$$

$$\begin{aligned}\Delta k_s(f_a) = &\frac{K_s^2(f_a, R_0) \cdot c \cdot M(f_a)}{2} \\ &\cdot \left\{-\frac{\lambda \cdot \dot{k}_2 \cdot f_a^2}{4 \cdot f_c^2 \cdot k_{20}^2} + \frac{3 \cdot \lambda \cdot \left[\left(k_{10} \cdot \dot{k}_3 + k_{30} \cdot \dot{k}_1\right) \cdot k_{20} - 3 \cdot k_{10} \cdot k_{30} \cdot \dot{k}_2\right]}{8 \cdot f_c^2 \cdot k_{20}^4} \cdot f_a^2\right. \\ &+\frac{3 \cdot \lambda \cdot \left(2 \cdot k_{10} \cdot A_3 \cdot \dot{k}_1 - k_{10}^2 \cdot \dot{A}_3\right)}{32 \cdot f_c^2} \cdot f_a^2 + \frac{3 \cdot \lambda^2 \cdot \left(k_{20} \cdot \dot{k}_3 - 3 \cdot k_{30} \cdot \dot{k}_2\right)}{16 \cdot f_c^2 \cdot k_{20}^4} \cdot f_a^3 \\ &\left.+\frac{3 \cdot \lambda^2 \cdot \left(A_3 \cdot \dot{k}_1 - k_{10} \cdot \dot{A}_3\right)}{32 \cdot f_c^2} \cdot f_a^3 + \frac{3 \cdot \lambda^3 \cdot \dot{A}_3}{128 \cdot f_c^2} f_a^4\right\}\end{aligned} \tag{27}$$

$$\tau(f_a, R) = \frac{2 \cdot R}{c \cdot M(f_a)} \tag{28}$$

$$\tau(f_a, R_0) = \frac{2 \cdot R_0}{c \cdot M(f_a)} \tag{29}$$

Based on (25), we can know that the new FM factor $K_s(f_a, R)$ will be no longer a constant and can be approximated as linear term of target position, and it also depends on the high order term of azimuth Doppler frequency. The compensation of new FM factor $K_s(f_a, R)$ will be presented in Section 4.2 and Section 4.3 in detail.

6) In Equation (16), the sixth term is generated because of decoupling two-dimension frequency spectrum, and it has relation with the cubic term of range frequency and can be expressed as

$$\phi_3(f_a,R) = 2\cdot\pi\cdot\left[\begin{array}{l} -\frac{\lambda\cdot f_a^2}{8\cdot k_2\cdot f_c^3} - \frac{3\cdot\lambda\cdot k_1\cdot k_3}{16\cdot k_2^3\cdot f_c^3}\cdot f_a^2 - \frac{3\cdot\lambda\cdot k_1^2\cdot\left(9\cdot k_3^2-4\cdot k_2\cdot k_4\right)}{64\cdot k_2^5\cdot f_c^3}\cdot f_a^2 \\ -\frac{\lambda^2\cdot k_3\cdot f_a^3}{8\cdot k_2^3\cdot f_c^3} - \frac{\lambda^2\cdot k_1\cdot\left(9\cdot k_3^2-4\cdot k_2\cdot k_4\right)}{16\cdot k_2^5\cdot f_c^3}\cdot f_a^3 - \frac{5\cdot\lambda^3\cdot\left(9\cdot k_3^2-4\cdot k_2\cdot k_4\right)}{256\cdot k_2^5\cdot f_c^3}\cdot f_a^4 \end{array}\right] \tag{30}$$

$\phi_3(f_a,R)$ has spatial variance, but its variation along range direction is small enough so as to be ignored, thus we can use $\phi_3(f_a,R_0)$ instead of $\phi_3(f_a,R)$ in general. It should be noted that the spatial variant phase in (30) must be compensated in two-dimension frequency domain, or else it will result in asymmetrical side-lobe in range direction after range compression.

4. IMPROVED NONLINEAR CHIRP SCALING (NCS) ALGORITHM

4.1. Reference Point RCM Correction and Cubic Phase Error Compensation

First of all, through range FFT and azimuth FFT, the two-dimension frequency spectrum is obtained. In two-dimension frequency domain, we can implement two steps. The first step is to remove the migration phase $b(f_a,f_r)$ at reference point through compensation function shown in (31). The second step is to multiply a nonlinear frequency-modulated function shown in (32), this function can not only remove the effect of cubic phase, but also remove the residual cubic phase error caused by adjusting the spatial variance of FM rate.

$$H_1 = \exp\left[\mathbf{j}\cdot 2\cdot\pi\cdot b(f_a,f_r)\right] \tag{31}$$

$$H_2 = \exp\left[\mathbf{j}\cdot\frac{2\cdot\pi}{3}\cdot Y(f_a)\cdot f_r^3\right] \tag{32}$$

where

$$Y(f_a) = \frac{\Delta k_s(f_a)\cdot(\alpha-0.5)}{K_s^3(f_a,R_0)\cdot(\alpha-1)} - \frac{3}{2\cdot\pi}\cdot\phi_3(f_a,R_0) \tag{33}$$

$$\alpha = \frac{M(f_{ref})}{M(f_a)} \tag{34}$$

f_{ref} is azimuth reference doppler frequency and depends on reference target position.

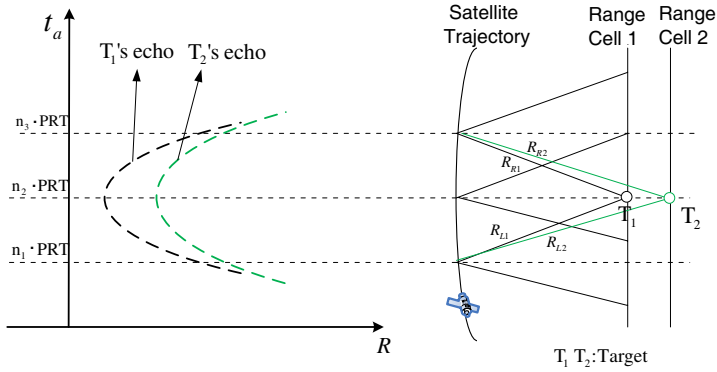

Figure 9. Diagrammatic sketch of the received echo data.

After compensation with (31) and (32), two-dimension frequency spectrum can be written as:

$$S_1(f_r, f_a) = u_r\left(\frac{f_r}{K_r}\right)\cdot u_a\left[f_a + \frac{2k_1}{c}(f_r + f_c)\right]\cdot\exp\left[\mathbf{j}\cdot 2\cdot\pi\cdot\phi_{az}(f_a, R)\right]$$
$$\cdot\exp\left[\mathbf{j}\cdot 2\cdot\pi\cdot\phi_{RP}(R)\right]\cdot\exp\left[-\mathbf{j}\cdot\frac{4\cdot\pi\cdot R}{c\cdot M(f_a)}\cdot f_r\right]$$
$$\cdot\exp\left[-\mathbf{j}\cdot\pi\cdot\frac{f_r^2}{K_s(f_a, R)}\right]\cdot\exp\left[\mathbf{j}\cdot\frac{2\cdot\pi}{3}\cdot Y_m(f_a)\cdot f_r^3\right] \quad (35)$$

where

$$Y_m(f_a) = \frac{\Delta k_s(f_a)\cdot(\alpha - 0.5)}{K_s^3(f_a, R_0)\cdot(\alpha - 1)} \quad (36)$$

4.2. RCM Space-variance Adjustment and FM Rate Space-variance Adjustment

As shown by the diagrammatic sketch of the received echo data in Fig. 9, T_1 and T_2 are in different range cells (range positions). On Fig. 9(a), the black and green dotted curves respectively stand for the echo positions of T_1 and T_2. The slant range histories of targets T_1 and T_2 are of nonlinear variance. Thus, the curved degree of the black dotted curve is different from that of the green dotted curve. The Nonlinear Chirp Scaling (NCS) algorithm is designed to adjust such different curved degrees to the same, then uniformly correct the range cell migration in 2-D frequency domain.

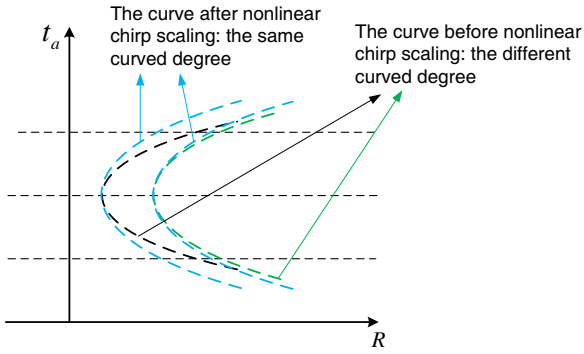

Figure 10. Diagrammatic sketch after nonlinear CS operation.

Via range IFFT to (35), Range-Doppler domain can be written as

$$S_1(t_r, f_a) = \mathbf{u}_r\left\{\frac{K_s(f_a, R)}{K_r}\left[t_r - \frac{2\cdot R}{c\cdot M(f_a)}\right]\right\}\cdot \mathbf{u}_a(f_a)\cdot\exp[\mathbf{j}\cdot 2\cdot\pi\cdot\phi_{az}(f_a, R)]$$
$$\cdot\exp\left[\mathbf{j}\cdot 2\cdot\pi\cdot\phi_{RP}(R)\right]\cdot\exp\left\{\mathbf{j}\cdot\pi\cdot K_s(f_a, R)\left[t_r - \frac{2\cdot R}{c\cdot M(f_a)}\right]^2\right\}$$
$$\cdot\exp\left\{\mathbf{j}\cdot\frac{2\cdot\pi}{3}\cdot Y_m(f_a)\cdot K_s(f_a, R)\left[t_r - \frac{2\cdot R}{c\cdot M(f_a)}\right]^3\right\}. \quad (37)$$

In order to remove spatial variance of range cell migration and range FM rate, nonlinear CS operation is implemented in range-doppler domain. After multiplying the compensation function (38) in range-doppler domain, the spatial variance of target range cell migration in whole scene is completely removed. Thus, the residual range cell migration can be bulk processed in two-dimension frequency domain. Fig. 10 is the comparable diagrammatic sketch before and after nonlinear CS operation.

The NCS compensation function can be expressed as

$$H_3 = \exp\left\{\mathbf{j}\cdot\pi\cdot q_2\cdot[t_r - \tau(f_a, R_0)]^2\right\}$$
$$\cdot\exp\left\{\mathbf{j}\cdot\frac{2\cdot\pi}{3}\cdot q_3\cdot[t_r - \tau(f_a, R_0)]^3\right\} \quad (38)$$

where

$$q_2 = K_s(f_a, R_0)\cdot(\alpha - 1) \quad (39)$$
$$q_3 = \frac{\Delta k_s(f_a)\cdot(\alpha - 1)}{2}. \quad (40)$$

The detailed derivation of q_2 and q_3 is shown in Appendix B.

4.3. RCMC, Range Compression and Secondary Range Compression

Multiplying Equation (37) with Equation (38), and implementing range FFT, the two-dimension frequency domain can be further rewritten as:

$$\begin{aligned} S_2(f_r, f_a) \;=\; & \mathbf{u}_r\left\{\frac{f_r}{K_s(f_a, R_0)\cdot\alpha}\right\}\cdot\mathbf{u}_a(f_a)\cdot\exp\left[\mathbf{j}\cdot 2\cdot\pi\cdot\varphi_{az}(f_a, R)\right] \\ & \cdot\exp\left[\mathbf{j}\cdot 2\cdot\pi\cdot\varphi_{RP}(R)\right]\cdot\exp\left[-\mathbf{j}\cdot\pi\cdot\frac{f_r^2}{\alpha\cdot K_s(f_a, R_0)}\right] \\ & \cdot\exp\left\{\mathbf{j}\cdot\frac{2\cdot\pi}{3}\cdot\frac{\left[Y_m(f_a)\cdot K_s^3(f_a, R_0)+q_3\right]}{\left[\alpha\cdot K_s(f_a, R_0)\right]^3}\cdot f_r^3\right\} \\ & \cdot\exp\left\{-\mathbf{j}\cdot\frac{4\cdot\pi\cdot R_0}{c}\cdot\left[\frac{1}{M(f_a)}-\frac{1}{M(f_{ref})}\right]\cdot f_r\right\} \\ & \exp\left[-\mathbf{j}\cdot\frac{4\cdot\pi\cdot R}{c\cdot M(f_{ref})}\cdot f_r\right]\cdot\exp\left(\mathbf{j}\cdot\pi\cdot C_0\right). \end{aligned} \tag{41}$$

In (41), C_0 in last term is the residual term after solving $Y_m(f_a)$, q_2 and q_3, and it can be expressed as:

$$\begin{aligned} C_0 = & K_s(f_a, R)\cdot\Delta\tau^2\cdot\left(\frac{1}{\alpha}-1\right)^2+\frac{2}{3}\cdot Y_m(f_a)\cdot K_s^3(f_a, R)\cdot\Delta\tau^3\cdot\left(\frac{1}{\alpha}-1\right)^3 \\ & +q_2\cdot\left(\frac{\Delta\tau}{\alpha}\right)^2+\frac{2}{3}\cdot q_3\cdot\left(\frac{\Delta\tau}{\alpha}\right)^3 \end{aligned} \tag{42}$$

$$\Delta\tau = \tau(f_a, R)-\tau(f_a, R_0). \tag{43}$$

C_0 not only relates to azimuth Doppler frequency, but also changes along range direction, thus the compensation of C_0 must be implemented in range-doppler domain.

After the nonlinear CS operation with (38), RCMC can be bulk processed in azimuth frequency domain. Therefore, the corresponding range compression and secondary range compression will be carried out in two-dimension frequency domain at the same time. The RCMC function can be written as

$$H_4 = \exp\left\{\mathbf{j}\cdot\frac{4\cdot\pi\cdot R_0}{c}\cdot\left[\frac{1}{M(f_a)}-\frac{1}{M(f_{ref})}\right]\cdot f_r\right\} \tag{44}$$

Figure 11 is the diagrammatic sketch after RCMC where the red and blue dotted lines stand for the same range cell, and the echo of targets is not compressed.

Furthermore, the range compression function and secondary range compression function can be expressed respectively as

$$H_5 = \exp\left[\mathbf{j}\cdot\pi\cdot\frac{f_r^2}{\alpha\cdot K_s\left(f_a,R_0\right)}\right]. \tag{45}$$

$$H_6 = \exp\left\{-\mathbf{j}\cdot\frac{2\cdot\pi}{3}\cdot\frac{\left[Y_m\left(f_a\right)\cdot K_s^3\left(f_a,R_0\right)+q_3\right]}{\left[\alpha\cdot K_s\left(f_a,R_0\right)\right]^3}\cdot f_r^3\right\}. \tag{46}$$

After processing with Equations (44), (45) and (46), the two-dimension frequency domain expression can be further written as

$$S_3\left(f_r,f_a\right)=\mathbf{u}_r\left\{\frac{f_r}{K_s\left(f_a,R_0\right)\cdot\alpha}\right\}\cdot u_a\left(f_a\right)\cdot\exp\left[\mathbf{j}\cdot 2\cdot\pi\cdot\phi_{az}\left(f_a,R\right)\right]$$
$$\cdot\exp[\mathbf{j}\cdot 2\cdot\pi\cdot\phi_{RP}\left(R\right)]\cdot\exp\left[-\mathbf{j}\cdot\frac{4\cdot\pi\cdot R}{c\cdot M\left(f_{ref}\right)}\cdot f_r\right]\cdot\exp\left(\mathbf{j}\cdot\pi\cdot C_0\right). \tag{47}$$

4.4. Azimuth Compression and Residual Phase Compensation

After RCMC and range compression, the echo can be well focused in the range direction. In sequence, the following processing should be azimuth compression, but the azimuth reference function should be updated along range direction. Thus, we should transform the echo data in (47) into the range-doppler domain. Implementing Inverse FFT (IFFT) to Equation (47) along range direction, the range-doppler

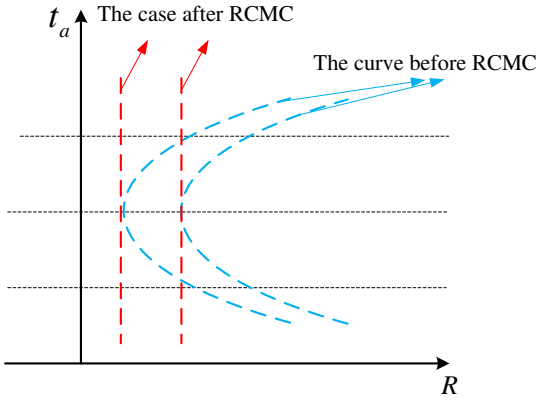

Figure 11. Diagrammatic sketch after RCMC.

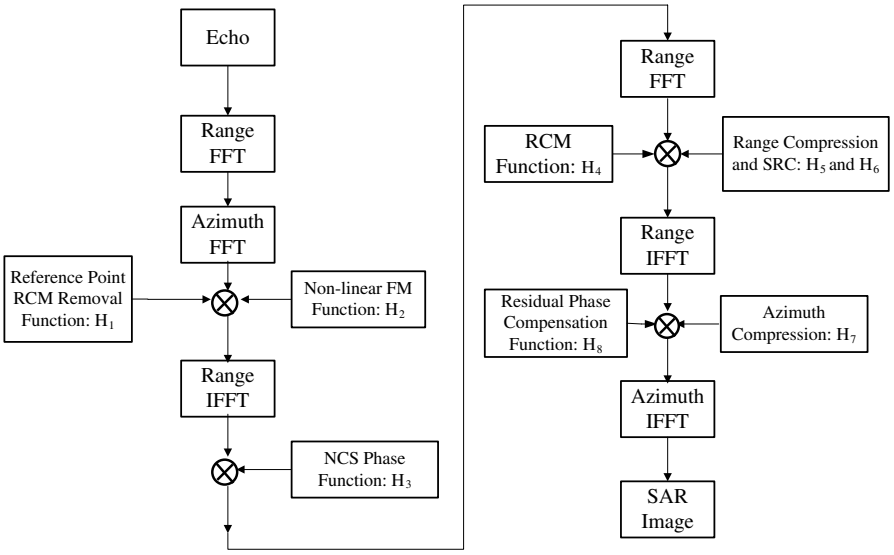

Figure 12. Improved NCS algorithm flow-chart in GEO SAR.

domain expression can be written as

$$S_3(t_r, f_a) = \sin c\left[t_r - \frac{2 \cdot R}{c \cdot M(f_{ref})}\right] \cdot u_a(f_a) \cdot \exp[\mathbf{j} \cdot 2 \cdot \pi \cdot \phi_{az}(f_a, R)] \cdot \exp[\mathbf{j} \cdot 2 \cdot \pi \cdot \phi_{RP}(R)] \cdot \exp(\mathbf{j} \cdot \pi \cdot C_0). \quad (48)$$

In sequence, azimuth compression should be implemented, and azimuth compression function can be written as

$$H_7 = \exp[-\mathbf{j} \cdot 2 \cdot \pi \cdot \phi_{az}(f_a, R)]. \quad (49)$$

In addition, the phase residual term also should be removed with (50) in range-doppler domain. According to (48), the residual phase expression can be written as

$$H_8 = \exp[-\mathbf{j} \cdot 2 \cdot \pi \cdot \phi_{RP}(R) - \mathbf{j} \cdot \pi \cdot C_0]. \quad (50)$$

After azimuth compression and residual phase compensation, the last step is azimuth IFFT and the focused image will be obtained.

4.5. Summary

As shown by the improved NCS algorithm flow-chart in GEO SAR in Fig. 12, the differences between the improved NCS algorithm and conventional NCS algorithm are marked with the red capital letters.

Table 2. Comparison of the key procedures between conventional NCS algorithm and improved NCS algorithm.

	Conventional NCS Algorithm	**Improved NCS Algorithm**
NCS Factor	$\frac{1}{\sqrt{1-\left(\frac{\lambda f_a}{2v}\right)^2}}-1$	$\frac{1}{\left\{\begin{array}{l}-\frac{\left(3\cdot k_{10}^2\cdot k_{30}\cdot\dot{k}_1+k_{10}^3\cdot\dot{k}_3\right)\cdot k_{20}-3\cdot k_{10}^3\cdot k_{30}\cdot\dot{k}_2}{8\cdot k_{20}^4} \\ +\left\{\frac{3\cdot\lambda^2\cdot\left(2\cdot k_{10}\cdot A_3\cdot\dot{k}_1-k_{10}^2\cdot\dot{A}_3\right)}{128}-\frac{\lambda^2\cdot\dot{k}_2}{16\cdot k_{20}^2}\right\}\cdot f_a^2 \\ +\left\{\frac{3\cdot\lambda^2\cdot\left[\left(k_{10}\cdot\dot{k}_3+k_{30}\cdot\dot{k}_1\right)\cdot k_{20}-3\cdot k_{10}\cdot k_{30}\cdot\dot{k}_2\right]}{32\cdot k_{20}^4}\right\}\cdot f_a^2 \\ +\left[\frac{\lambda^3\cdot\left(k_{20}\cdot\dot{k}_3-3\cdot k_{30}\cdot\dot{k}_2\right)}{32\cdot k_{20}^4}+\frac{\lambda^3\cdot\left(A_3\cdot\dot{k}_1-k_{10}\cdot\dot{A}_3\right)}{64}\right]\cdot f_a^3 \\ -\frac{k_{10}\cdot k_{20}\cdot\dot{k}_1-k_{10}^2\cdot\dot{k}_2}{2\cdot k_{20}^2} \\ +\frac{3\cdot\lambda^3\cdot\dot{A}_3}{1024}\cdot f_a^4-\frac{A_3\cdot\dot{k}_1-k_{10}\cdot\dot{A}_3}{64}+1\end{array}\right.}$ Where A_3 and $\dot{A}_3$ are shown as Equations (21) and (22) respectively.
Chirp Frequency Modulation Rate	$\frac{1}{\frac{1}{K_r}-\frac{2\cdot R\cdot\lambda\cdot\left(\frac{\lambda f_a}{2v}\right)^2}{c^2\cdot\left[1-\left(\frac{\lambda f_a}{2v}\right)^2\right]^{\frac{3}{2}}}}$	$\frac{1}{\left\{\begin{array}{l}-\left[\frac{\lambda}{4\cdot k_2\cdot f_c^2}+\frac{3\cdot\lambda\cdot k_1\cdot k_3}{8\cdot k_2^3\cdot f_c^2}+\frac{3\cdot\lambda\cdot k_1^2\cdot\left(9\cdot k_3^2-4\cdot k_2\cdot k_4\right)}{32\cdot k_2^5\cdot f_c^2}\right]\cdot f_a^2 \\ -\left[\frac{3\cdot\lambda^2\cdot k_3}{16\cdot k_2^3\cdot f_c^2}+\frac{3\cdot\lambda^2\cdot k_1\cdot\left(9\cdot k_3^2-4\cdot k_2\cdot k_4\right)}{32\cdot k_2^5\cdot f_c^2}\right]\cdot f_a^3 \\ -\frac{3\cdot\lambda^3\cdot\left(9\cdot k_3^2-4\cdot k_2\cdot k_4\right)}{128\cdot k_2^5\cdot f_c^2}\cdot f_a^4+\frac{1}{K_r}\end{array}\right.}$
Modulation Phase in Azimuth	$2\cdot\pi\cdot\frac{R_c}{v}\cdot\sqrt{\left(\frac{2\cdot v}{\lambda}\right)^2-f_a^2}$	$2\pi\cdot\left\{\begin{array}{l}\left[\frac{k_1}{2\cdot k_2}+\frac{3\cdot k_1^2\cdot k_3}{8\cdot k_2^3}+\frac{k_1^3\cdot\left(9\cdot k_3^2-4\cdot k_2\cdot k_4\right)}{16\cdot k_2^5}\right]\cdot f_a \\ +\left[\frac{\lambda}{8\cdot k_2}+\frac{3\cdot\lambda\cdot k_1\cdot k_3}{16\cdot k_2^3}+\frac{3\cdot\lambda\cdot k_1^2\cdot\left(9\cdot k_3^2-4\cdot k_2\cdot k_4\right)}{64\cdot k_2^5}\right]\cdot f_a^2 \\ +\left[\frac{\lambda^2\cdot k_3}{32\cdot k_2^3}+\frac{\lambda\cdot k_1\cdot\left(9\cdot k_3^2-4\cdot k_2\cdot k_4\right)}{64\cdot k_2^5}\right]\cdot f_a^3 \\ +\frac{\lambda^3\cdot\left(9\cdot k_3^2-4\cdot k_2\cdot k_4\right)}{512\cdot k_2^5}\cdot f_a^4\end{array}\right.$

Based on Equations (31) to (50), the NCS focusing algorithm of curved trajectory in GEO SAR has been completely presented. Compared with conventional NCS algorithm under linear trajectory in LEO SAR, the big differences in GEO SAR NCS algorithm are from the compensation factors in Equations (17), (23), (25), (36), (39), (40), etc. Table 2 shows the comparison results of the conventional NCS algorithm and the improved NCS algorithm.

Table 3. Simulation parameters.

Parameter	Value	Unit
Sampling frequency	20	MHz
Bandwidth	18	MHz
Wavelength	0.09375	m
Pulse width	20	us
Pulse Repetition Frequency (PRF)	200	Hz
Synthetic aperture time	100	s

5. SIMULATION RESULTS

5.1. The Imaging Verification of Point Target

In this section, we will verify the improved NCS algorithm through point target imaging. The simulation parameters are listed in Table 3.

Here, we will compare the results between the improved NCS algorithm and the conventional NCS algorithm in GEO SAR Perigee. In order to use linear trajectory model, we need to get equivalent velocity and equivalent squint angle, thus satellite trajectory parameters are used to estimate the Doppler centroid frequency f_{dc} and the Doppler FM rate f_{dr}. Substituting f_{dc} and f_{dr} into (51), equivalent velocity and equivalent squint angle can be obtained. Then, the conventional NCS algorithm can be used in Perigee.

$$\begin{cases} v = \sqrt{\left(\frac{f_{dc}\cdot\lambda}{2}\right)^2 - \frac{f_{dr}\cdot R_0\cdot\lambda}{2}} \\ \theta = \arcsin\left(\frac{f_{dc}\cdot\lambda}{2\cdot v}\right) \end{cases} . \tag{51}$$

The imaging results of point target in (5 km, 5 km) are shown in Fig. 13, because of the effect of curved trajectory, the conventional NCS algorithm defocused in azimuth direction (in Fig. 13(b)), while the improved NCS algorithm is focused very well in azimuth direction (in Fig. 13(a)). Therefore, the effectiveness of improved NCS algorithm for curved trajectory is verified.

5.2. The Imaging Verification of Point Array Targets

In order to further prove the effectiveness of the improved NCS algorithm under long aperture time and large scene focusing, the imaging target scenes are set as the size of 100 km × 100 km in Apogee and Perigee respectively, there are total 121 point targets uniformity distributed in the whole scene, the separation between point targets is

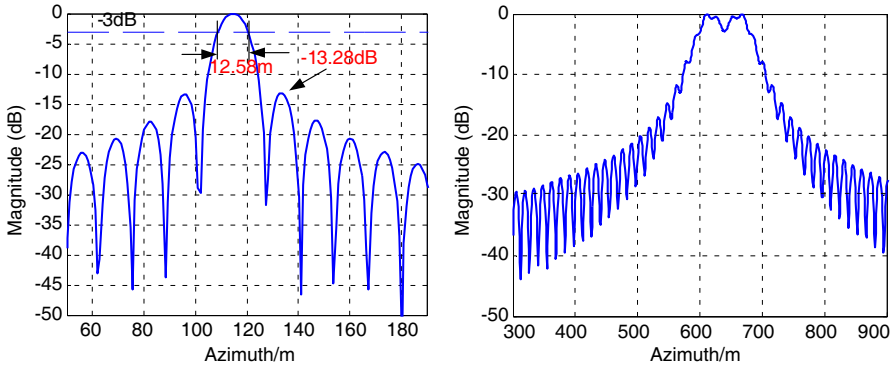

Figure 13. Azimuth compression profile of target position (5 km, 5 km). (a) Azimuth profile of improved NCS. (b) Azimuth profile of conventional NCS.

10 km in azimuth direction and range direction. The imaging results with improved NCS algorithm in Perigee and Apogee are shown in Fig. 14 and Fig. 15 respectively.

In order to evaluate the correctness of imaging results, some special point targets in different positions are chosen to calculate the evaluation results, such as Peak Side-Lobe Ratio (PSLR) and Integration Side-Lobe Ratio (ISLR). In theory, the PSLR and ISLR are -13.2 dB and -10 dB respectively under the condition of rectangular window function, the evaluation results from imaging results are shown in Table 4 and coincident with theoretic value completely, no matter in Perigee and in Apogee. Furthermore, based on the signal bandwidth and synthetic aperture time, the range resolution and azimuth resolution in Apogee and Perigee are approximate to 7.38 m and 12.71 m in theory respectively, the evaluation results are also coincident with theoretic value as shown in Table 4. Deserving to attention that conventional NCS algorithm can't be used for imaging Apogee in GEO SAR because of abnormal slant range history shown in Fig. 6(b), while the improved NCS algorithm obtain satisfactory imaging results shown in Fig. 15.

In order to compare the imaging results between improved NCS algorithm and conventional NCS algorithm, the imaging results through conventional NCS algorithm in Perigee are shown in Fig. 16. The target scenes are set as the size of 100 km $\times$ 100 km and the simulation parameters are the same with the improved NCS algorithm. From the range and azimuth profiles in Fig. 16, it is obvious that the defocusing appears in the azimuth profile except the scene center,

Table 4. Evaluation results of improved NCS algorithm.

Point target position/km		PSLR/dB		ISLR/dB		Resolution/m	
		Range	Azimuth	Range	Azimuth	Range	Azimuth
GEO SAR Perigee	(0, 0)	−13.28	−13.28	−10.06	−10.21	7.38	12.54
	(−10, 10)	−13.22	−13.22	−9.94	−10.11	7.39	12.66
	(20, −20)	−13.17	−13.11	−9.97	−10.09	7.40	12.59
	(30, 30)	−13.25	−13.09	−10.05	−10.24	7.38	12.59
	(−50,−50)	−13.21	−13.01	−10.38	−10.15	7.39	12.62
GEO SAR Apogee	(0, 0)	−13.12	−13.25	−9.93	−10.36	7.41	12.69
	(−10, 10)	−13.25	−13.25	−10.09	−10.23	7.37	12.73
	(20, −20)	−13.12	−13.19	−9.89	−10.34	7.39	12.73
	(30, 30)	−13.22	−13.19	−10.03	−10.34	7.39	12.58
	(−50,−50)	−13.15	−13.17	−9.94	−10.39	7.40	12.63

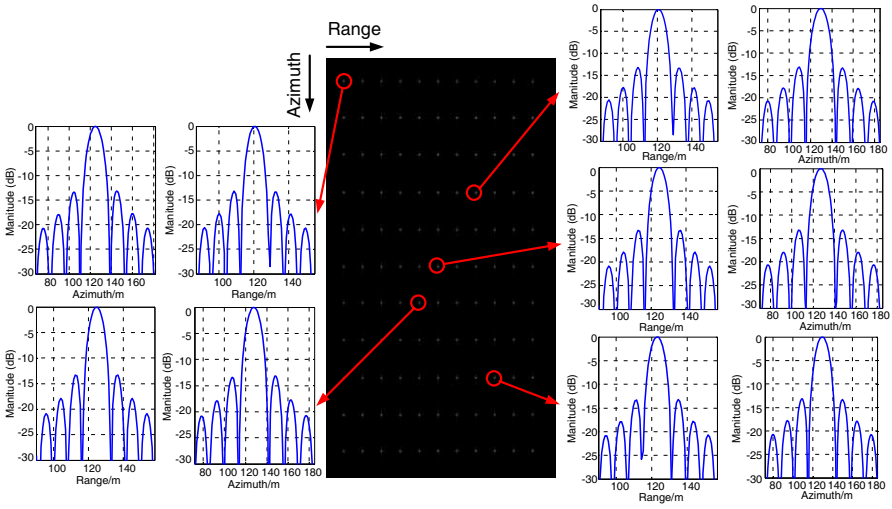

Figure 14. Imaging results in Perigee through improved NCS algorithm (100 km × 100 km size).

and the defocusing level increases with the increase of the separation distance between the target and the scene center. However, the improved NCS algorithm can focus the whole scene very well, the results are shown in Fig. 14 and Fig. 15.

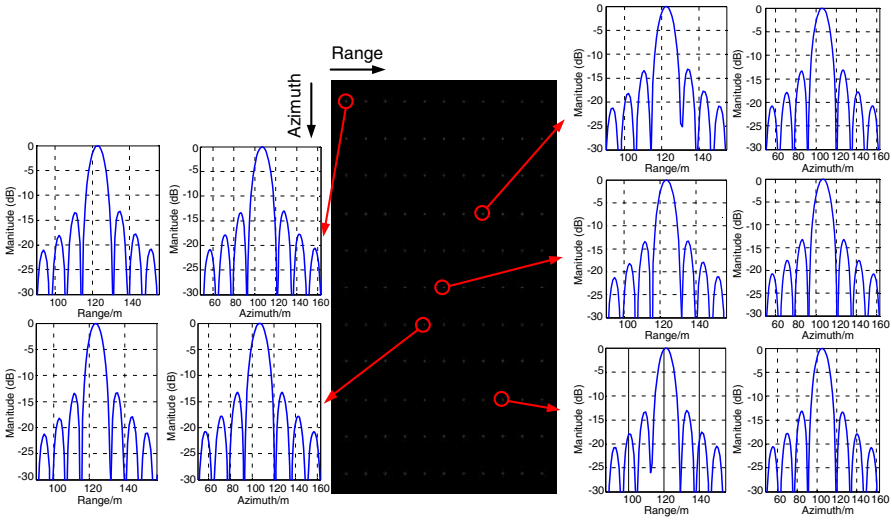

Figure 15. Imaging results in Apogee through improved NCS algorithm (100 km × 100 km size).

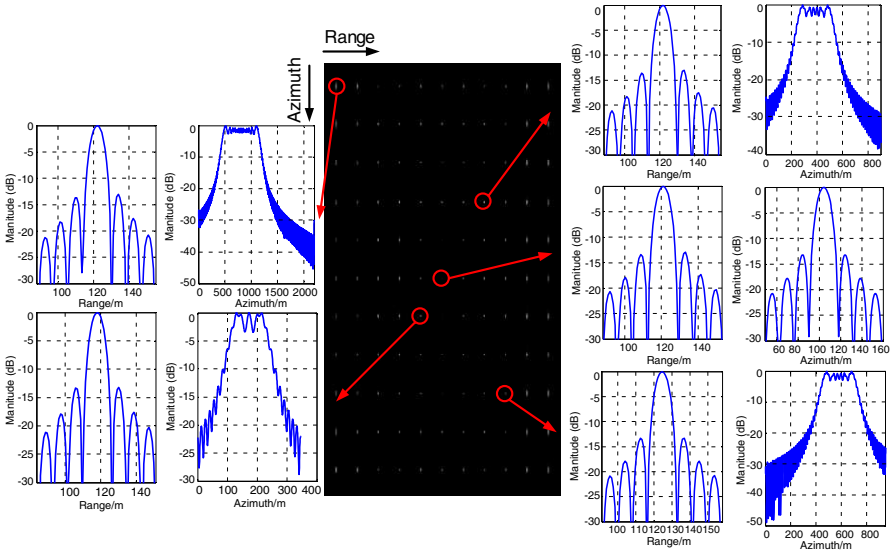

Figure 16. Imaging results in Perigee through conventional NCS algorithm.

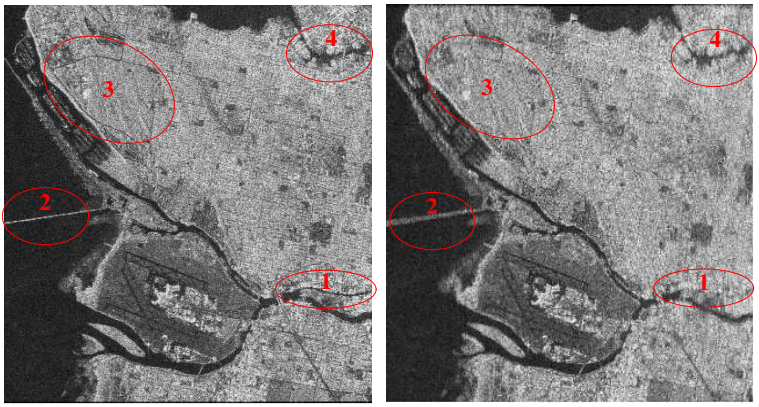

(a) (b)

Figure 17. The comparison of imaging results of Vancouver area. (a) Improved NCS algorithm. (b) Conventional NCS algorithm.

5.3. The Imaging Verification of Area Targets

In order to further verify the correctness of improved NCS algorithm, we use the real SAR image (Vancouver area from RadarSat-1) as the input Radar Cross Section (RCS) information in echo generation, the orbit parameters used in GEO SAR are listed in Table 1, the radar parameters used in GEO SAR are listed in Table 3. The improved NCS algorithm and conventional NCS algorithm both are used for focusing the echo data, the imaging results are shown in Fig. 17. As we can see from Fig. 17, it is obvious that the well focused result by improved NCS can be clearly seen and is shown in Fig. 17(a), but the conventional NCS algorithm results in the defocusing in Fig. 17(b). Let's move into detailed explanations about the images. In Fig. 17(b), in the area 1 with red ellipse, the river disappeared. In the area 2, we can see a long line, but it was very rough and obviously defocusing. In area 3, the road near the building was masked because of the defocusing of strong building. In area 4, the river became fuzzy and was the same with area 3. However, in Fig. 17(a), we can see a clear river in area 1, we can see a thin and bright line in area 2 and it is obvious to stand for a bridge. At the same time, we can see some roads and river clearly in area 3 and area 4. All these results were shown that the improved NCS algorithm focused the echo very well.

6. CONCLUSION

Because of large orbit height in GEO SAR, the angular velocity of earth rotation is nearly equal to that of satellite, and the rotation direction is different. Meanwhile, the satellite relative velocity and beam velocity change a lot and have large differences such as several times (six or more than ten). Therefore, these complex factors result in complex synthetic aperture trajectory and target phase histories. Therefore, the LEO SAR imaging algorithms lose effect in GEO SAR. In this paper, the error of linear trajectory model in GEO SAR is discussed in detail. Besides, the NCS algorithm based on curved trajectory model is analytically derived in GEO SAR. Furthermore, some new NCS compensation factors are presented. Finally, based on the point array targets and the real image of Vancouver area, the simulation results verify the correctness of the improved NCS algorithm completely, and the imaging results of 10 m × 10 m (Range × Azimuth) resolution are obtained in GEO SAR Apogee and Perigee. In addition, the effects of orbit perturbation and ionosphere on image formation are also very important factors, which will be the major work in the future.

APPENDIX A. EXPRESSION OF TWO-DIMENSIONAL FREQUENCY SPECTRUM

The two-dimension frequency spectrum of the echo will be derived based on the series reversion method in [41], but the difference in GEO SAR is the curved trajectory model instead of bistatic slant range model. Firstly, the expression of received echo data can be expressed as

$$s(t_r, t_a) = \mathbf{u}_r\left(t_r - \frac{2\cdot R_n}{c}\right)\cdot \mathbf{u}_a(t_a)\cdot \exp\left[\mathbf{j}\cdot\pi\cdot K_r\cdot\left(t_r - \frac{2\cdot R_n}{c}\right)^2\right] \cdot \exp\left(-\mathbf{j}\cdot\frac{4\cdot\pi\cdot R_n}{\lambda}\right) \tag{A1}$$

After range FFT, we can obtain

$$s(f_r, t_a) = u_r\left(\frac{f_r}{K_r}\right)\cdot u_a(t_a)\cdot\exp\left(-\mathbf{j}\cdot\pi\cdot\frac{f_r^2}{K_r}\right) \cdot\exp\left[-\mathbf{j}\cdot\frac{4\cdot\pi\cdot R_n}{c}\cdot(f_c+f_r)\right] \tag{A2}$$

Because R_n is shown as the format of Taylor series expansion, it is difficult to obtain the stationary phase point through POSP, but

the series reversion principle can be used for solving stationary phase. Based on (A2) and (2), we have

$$s\left(f_r, t_a\right) = s_1\left(f_r, t_a\right) \cdot \exp\left[-\mathbf{j} \cdot \frac{4 \cdot \pi \cdot k_1 \cdot t_a \cdot (f_c + f_r)}{c}\right] \tag{A3}$$

We first solve the two-dimension frequency spectrum expression of $s_1\left(f_r, t_a\right)$, and then solve the two-dimension frequency spectrum expression of $s\left(f_r, t_a\right)$ by using expression (A4)

$$\begin{aligned} & s_1\left(f_r, t_a\right) \cdot \exp\left[-\mathbf{j} \cdot \frac{4 \cdot \pi \cdot k_1 \cdot t_a \cdot (f_c + f_r)}{c}\right] \\ \Leftrightarrow\ & S_1\left(f_r, f_a + \frac{2 \cdot k_1 \cdot (f_c + f_r)}{c}\right) \end{aligned} \tag{A4}$$

The integral phase of $s_1\left(f_r, t_a\right)$ can be written as

$$\Psi = -\pi \cdot \frac{f_r^2}{K_r} - \frac{4 \cdot \pi \cdot (f_c + f_r)}{c} \cdot \left(k_1 \cdot t_a + k_2 \cdot t_a^2 + k_3 \cdot t_a^3 + k_4 \cdot t_a^4\right) - 2 \cdot \pi \cdot f_a \cdot t_a \tag{A5}$$

Define $\frac{d\Psi}{dt_a} = 0$, we have

$$-\frac{c \cdot f_a}{2 \cdot (f_r + f_c)} = 2 \cdot k_2 \cdot t_a + 3 \cdot k_3 \cdot t_a^2 + 4 \cdot k_4 t_a^3 \tag{A6}$$

Using series reversion principle, we can define

$$t_a = F_1 \cdot \left[-\frac{c \cdot f_a}{2 \cdot (f_r + f_c)}\right] + F_2 \cdot \left[-\frac{c \cdot f_a}{2 \cdot (f_r + f_c)}\right]^2 + F_3 \cdot \left[-\frac{c \cdot f_a}{2 \cdot (f_r + f_c)}\right]^3 + \ldots \tag{A7}$$

Substituting (A7) into (A6), we can obtain

$$\begin{aligned} F_1 &= 1/[2 \cdot k_2] \\ F_2 &= -k_3/\left[8 \cdot k_2^3\right] \\ F_3 &= \left[9 \cdot k_3^2 - 4 \cdot k_2 \cdot k_4\right]/\left(16 \cdot k_2^5\right) \end{aligned} \tag{A8}$$

So the expression of two-dimension frequency spectrum can be expressed as

$$\begin{aligned} S\left(f_r, f_a\right) = {} & \mathbf{u}_r\left(\frac{f_r}{K_r}\right) \cdot \mathbf{u}_a\left[f_a + \frac{2 \cdot k_1}{c} \cdot (f_r + f_c)\right] \cdot \exp\left(-\mathbf{j} \cdot \pi \cdot \frac{f_r^2}{K_r}\right) \\ & \exp\left\{\mathbf{j} \cdot 2 \cdot \pi \cdot \left[-\frac{2 \cdot (f_r + f_c)}{c} \cdot R + \frac{1}{4 \cdot k_2} \cdot \left(\frac{c}{2 \cdot (f_r + f_c)}\right) \cdot \left(f_a + \frac{2 \cdot k_1}{c} \cdot (f_r + f_c)\right)^2\right.\right. \\ & + \frac{k_3}{8 \cdot k_2^3} \cdot \left(\frac{c}{2 \cdot (f_r + f_c)}\right)^2 \cdot \left(f_a + \frac{2 \cdot k_1}{c} \cdot (f_r + f_c)\right)^3 \\ & \left.\left. + \frac{9 \cdot k_3^2 - 4 \cdot k_2 \cdot k_4}{64 \cdot k_2^5} \cdot \left(\frac{c}{2 \cdot (f_r + f_c)}\right)^3 \cdot \left(f_a + \frac{2 \cdot k_1}{c} \cdot (f_r + f_c)\right)^4\right]\right\} \end{aligned} \tag{A9}$$

where f_r and f_a are the range frequency and azimuth frequency, $\mathbf{u}_r(\cdot)$ and $\mathbf{u}_a(\cdot)$ the envelopes in range direction and azimuth direction, K_r the Frequency-Modulated (FM) rate, and c the light speed.

According to (A9), as we can see that there is serious coupling between range direction and azimuth direction in two-dimension frequency spectrum, thus it is necessary to decouple and compensate spatial variation if we want to focus large scene. Using Equation (A10), we can further expand the two-dimension frequency spectrum.

$$\begin{aligned}
&\frac{1}{f_r+f_c}=\frac{1}{f_c}\left[1-\frac{f_r}{f_c}+\left(\frac{f_r}{f_c}\right)^2-\left(\frac{f_r}{f_c}\right)^3+\ldots\right]\\
&\left(\frac{1}{f_r+f_c}\right)^2=\frac{1}{f_c^2}\left[1-\frac{2\cdot f_r}{f_c}+3\cdot\left(\frac{f_r}{f_c}\right)^2-4\cdot\left(\frac{f_r}{f_c}\right)^3+\ldots\right]\\
&\left(\frac{1}{f_r+f_c}\right)^3=\frac{1}{f_c^3}\left[1-\frac{3\cdot f_r}{f_c}+6\cdot\left(\frac{f_r}{f_c}\right)^2-10\cdot\left(\frac{f_r}{f_c}\right)^3+\ldots\right]. \qquad \text{(A10)}
\end{aligned}$$

Substituting (A10) into (A9), after derivation and simplification, we can obtain two-dimension frequency spectrum of GEO SAR as

$$\begin{aligned}
S(f_r,f_a)=&\mathbf{u}_r\left(\frac{f_r}{K_r}\right)\cdot\mathbf{u}_a\left[f_a+\frac{2k_1}{c}(f_r+f_c)\right]\cdot\exp\left[\mathbf{j}\cdot2\cdot\pi\cdot\phi_{az}(f_a,R)\right]\\
&\cdot\exp[\mathbf{j}\cdot2\cdot\pi\cdot\phi_{RP}(R)]\cdot\exp[-\mathbf{j}\cdot2\cdot\pi\cdot b(f_a,f_r)]\cdot\exp\left[-\mathbf{j}\cdot\frac{4\cdot\pi\cdot R}{c\cdot M(f_a)}\cdot f_r\right]\\
&\cdot\exp\left[-\mathbf{j}\cdot\pi\cdot\frac{f_r^2}{K_s(f_a,R)}\right]\cdot\exp\left[\mathbf{j}\cdot\phi_3(f_a,R)\cdot f_r^3\right] \qquad \text{(A11)}
\end{aligned}$$

APPENDIX B. GEO SAR NCS COMPENSATION FACTOR

After introducing a nonlinear FM function in two-dimensional frequency domain, via the range IFFT operation, the range-doppler expression can be written as

$$\begin{aligned}
S_1(t_r,f_a)=&\exp\left[\mathbf{j}\cdot2\cdot\pi\cdot\phi_{az}(f_a,R)\right]\cdot\exp\left[\mathbf{j}\cdot2\cdot\pi\cdot\phi_{RP}(R)\right]\\
&\cdot\exp\left\{\mathbf{j}\cdot\pi\cdot K_s(f_a,R)\left[t_r-\frac{2\cdot R}{c\cdot M(f_a)}\right]^2\right\}\\
&\cdot\exp\left\{\mathbf{j}\cdot\frac{2\cdot\pi}{3}\cdot Y_m(f_a)\cdot K_s(f_a,R)\left[t_r-\frac{2\cdot R}{c\cdot M(f_a)}\right]^3\right\} \qquad \text{(B1)}
\end{aligned}$$

Here, we ignore the effect of amplitude, and H_1 has been compensated in two-dimensional frequency domain in the derivation

of (B1). The nonlinear CS operation is implemented in range-doppler domain and the CS function can be expressed as

$$\begin{aligned} H_3 &= \exp\left\{\mathbf{j}\cdot\pi\cdot q_2\cdot\left[t_r-\tau\left(f_a,R_0\right)\right]^2\right\} \\ &\quad\cdot\exp\left\{\mathbf{j}\cdot\frac{2\cdot\pi}{3}\cdot q_3\cdot\left[t_r-\tau\left(f_a,R_0\right)\right]^3\right\} \end{aligned} \tag{B2}$$

After multiplying (B1) by (B2), we have

$$\begin{aligned} S\left(t_r,f_a\right) = &\exp\left[\mathbf{j}\cdot 2\cdot\pi\cdot\phi_{az}\left(f_a,R\right)\right]\cdot\exp\left[\mathbf{j}\cdot 2\cdot\pi\cdot\phi_{RP}\left(R\right)\right] \\ &\cdot\exp\left\{\mathbf{j}\cdot\pi\cdot\left[C_0+2\cdot C_1\cdot\left[t_r-\tau_s\left(f_a,R\right)\right]\right.\right. \\ &\left.\left.+C_2\cdot\left[t_r-\tau_s\left(f_a,R\right)\right]^2+\frac{2}{3}\cdot C_3\cdot\left[t_r-\tau_s\left(f_a,R\right)\right]^3\right]\right\} \end{aligned} \tag{B3}$$

where

$$\begin{aligned} C_1 &= \left[K_s\left(f_a,R_0\right)\cdot\left(\frac{1}{\alpha}-1\right)+\frac{q_2}{\alpha}\right]\cdot\Delta\tau+\left[\Delta k_s\left(f_a\right)\cdot\left(\frac{1}{\alpha}-1\right)\right. \\ &\quad\left.+Y_m\left(f_a\right)\cdot K_s^3\left(f_a,R_0\right)\cdot\left(\frac{1}{\alpha}-1\right)^2+\frac{q_3}{\alpha^2}\right]\cdot\Delta\tau^2+\ldots \end{aligned} \tag{B4}$$

$$\begin{aligned} C_2 &= \left[K_s\left(f_a,R_0\right)+q_2\right]+\left[\Delta k_s\left(f_a\right)\right. \\ &\quad\left.+2\cdot Y_m\left(f_a\right)\cdot K_s^3\left(f_a,R_0\right)\cdot\left(\frac{1}{\alpha}-1\right)+\frac{2\cdot q_3}{\alpha}\right]\cdot\Delta\tau+\ldots \end{aligned} \tag{B5}$$

$$C_3 = Y_m\left(f_a\right)\cdot K_s^3\left(f_a,R_0\right)+q_3+\ldots \tag{B6}$$

In order to adjust the spatial variance, we should define the following equation to exist.

$$\begin{cases} K_s\left(f_a,R_0\right)\cdot\left(\frac{1}{\alpha}-1\right)+\frac{q_2}{\alpha}=0 \\ \Delta k_s\left(f_a\right)\cdot\left(\frac{1}{\alpha}-1\right)+Y_m\left(f_a\right)\cdot K_s^3\left(f_a,R_0\right)\cdot\left(\frac{1}{\alpha}-1\right)^2+\frac{q_3}{\alpha^2}=0 \\ \Delta k_s\left(f_a\right)+2\cdot Y_m\left(f_a\right)\cdot K_s^3\left(f_a,R_0\right)\cdot\left(\frac{1}{\alpha}-1\right)+\frac{2\cdot q_3}{\alpha}=0 \end{cases} \tag{B7}$$

Solving (B7), we can obtain

$$\begin{cases} q_2 = K_s\left(f_a,R_0\right)\cdot(\alpha-1) \\ q_3 = \frac{\Delta k_s(f_a)\cdot(\alpha-1)}{2} \\ Y_m\left(f_a\right) = \frac{\Delta k_s(f_a)\cdot(\alpha-0.5)}{K_s(f_a,R_0)^3\cdot(\alpha-1)} \end{cases} \tag{B8}$$

ACKNOWLEDGMENT

This work was supported by the key project of the National Natural Science Foundation of China (Grant Nos. 61032009 and 61225005).

REFERENCES

1. Tomiyasu, K., "Synthetic aperture radar in geosynchronous orbit," *IEEE Antennas and Propagation Symp.*, 42–45, University of Maryland, May 1978.
2. Tomiyasu, K. and J. L. Pacelli, "Synthetic aperture radar imaging from an inclined geosynchronous orbit," *IEEE Trans. Geosci. Remote Sens.*, Vol. 21, 324–329, Jul. 1983.
3. Madsen, S. N., W. Edelstein, L. D. DiDomenico, and J. LabBrecque, "A geosynchronous synthetic aperture radar; for tectonic mapping, disaster management and measurements of vegetation and soil moisture," *Proc. IEEE IGARSS*, Vol. 1, 447–449, Jul. 2001.
4. Osipov, I. G., L. B. Neronskiy, V. I. Andrianov, et al., "Calculated performance of sar for high orbit spacecraft using nuclear power supply," *Proc. EUSAR*, 1–4, Germany, May 2006.
5. Moussessian, A., C. Chen, W. Edelstein, et al., "System concepts and technologies for high orbit SAR," *2005 IEEE MTT-S International Microwave Symposium Digest*, 1623–1626, 2005.
6. Madsen, S. N., C. Chen, and W. Edelstein, "Radar options for global earthquake monitoring," *Proc. IEEE IGARSS*, Vol. 3, 1483–1485, Jun. 2002.
7. NASA and JPL, "Global earthquake satellite system: A 20-year plan to enable earthquake prediction," JPL Document, 2003, http://solidearth.jpl.nasa.gov/GESS/3123_GESS_Rep_2003.pdf.
8. Prati, C., F. Rocca, D. Giancola, et al. "Passive geosynchronous SAR system reusing backscattered digital audio broadcasting signals," *IEEE Trans. Geosci. Remote Sens.*, Vol. 36, No. 6, 1973–1976, Nov. 1998.
9. Cazzani, L., C. Colesanti, D. Leva, et al., "A ground-based parasitic SAR experiment," *IEEE Trans. Geosci. Remote Sens.*, Vol. 38, No. 5, 1973–1976, Sep. 2000.
10. Edelstein, W., S. Madsen, A. Mooussessian, and C. Chen, "Concepts and technologies for synthetic aperture radar from MEO and geosynchronous orbits," *Proc. SPIE*, Vol. 5659, 195–203, 2005.
11. Moussessian, A., C. Chen, W. Edelstein, S. Madsen, and P. Rosen, "System concepts and technologies for high orbit SAR," *IEEE MTI-S International Microwave Symplosium*, 1623–1626, Long Beach, CA, USA, Jun. 2005.
12. Hobbs, S. E. and D. Bruno, "Radar imaging from geo: Challenges and applications," *Remote Sensing and Photogrammetry Society*

Annual Conf., 1–6, 2007.

13. Bruno, D. and S. E. Hobbs, "Radar imaging from geosynchronous orbit: Temporal decorrelation aspects," *IEEE Trans. Geosci. Remote Sens.*, Vol. 48, No. 7, 2924–2929, 2010.
14. Sheng, W. and S. E. Hobbs, "Research on compensation of motion, Earth curvature and tropospheric delay in GEO SAR," *Acta Astronautica*, Vol. 68, 2005–2011, 2011.
15. Hobbs, S. E., *GeoSAR Summary of the Group Design Project, MSc in Astronautics and Space Engineering 2005/06*, Cranfield University, 2006.
16. Kou, L. L., X. Q. Wang, J. S. Chong, and M. S. Xiang, "Research on interferometric deformation detection for geosynchronous SAR," *Proc. IGARSS*, 3502–3505, Hawaii, America, Jul. 2010.
17. Hu, C., F. F. Liu, W. F. Yang, T. Zeng, and T. Long, "Modification of slant range model and imaging processing in GEO SAR," *Proc. IGARSS*, 4679–4682, Hawaii, America, Jul. 2010.
18. Yang, W. F., Y. Zhu, F. F. Liu, C. Hu, and Z. G. Ding, "Modified range migration algorithm in GEO SAR system," *Proc. EUSAR,* 708–711, May 2010.
19. Liu, Q., W. Hong, W. X. Tan, Y. Lin, Y. Wang, and Y. Wu, "An improved polar format algorithm with performance analysis for geosynchronous circular SAR 2D imaging," *Progress In Electromagnetics Research*, Vol. 119, 155–170, 2011.
20. Liu, Q., W. Hong, W. X. Tan, and Y. Wu, "Efficient geosynchronous circular SAR raw data simulation of extended 3-D scenes," *Progress In Electromagnetics Research*, Vol. 127, 335–350, 2012.
21. Yu, Z., J. Chen, C. S. Li, et al., "Concepts, properties and imaging technologies for GEO SAR," *Proc. SPIE*, Vol. 7494, 749407-1–749407-8, 2009.
22. Long, T., X. C. Dong, C. Hu, and T. Zeng, "A new method of zero-doppler centroid control in GEO SAR," *IEEE Geosci. Romote Sens. Lett.*, Vol. 8, No. 3, 513–516, May 2011.
23. Knaell, K. K., "Three-dimensional SAR from curvilinear aperture," *Proc. SPIE*, Vol. 2230, 120–134, 1994.
24. Ishimaru, A., T. Chan, and Y. Kuga, "An imaging technique using confocal circular synthetic aperture radar," *IEEE Trans. Geosci. Remote Sens.*, Vol. 36, No. 5, 1524–1530, Sep. 1998.
25. Cantalloube, H. and E. C. Koeniquer, "High resolution SAR imaging along circular trajectories," *Proc. IGARSS*, 2259–2262,

Jul. 2007.

26. Soumekh, M., "Reconnaissance with slant plane circular SAR imaging," *IEEE Trans. Image Process.*, Vol. 5, No. 8, 1252–1265, Aug. 1996.
27. Burki, J. and C. F. Barnes, "Slant plane CSAR processing using householder transform," *IEEE Trans. Geosci. Remote Sens.*, Vol. 17, No. 10, 1900–1907, Oct. 2008.
28. Tian, W. M., C. Hu, and T. Zeng, "Several special issues in GEO SAR system" *8th European Conference on Synthetic Aperture Radar (EuSAR)*, 1–4, Jun. 7–10, 2010.
29. Hu, C., T. Long, T. Zeng, F. F. Liu, and Z. P. Liu, "The accurate focusing and resolution analysis method in geosynchronous SAR," *IEEE Trans. Geosci. Remote Sens.*, Vol. 49, No. 10, 1–16, Oct. 2011.
30. Liu, Z. P., C. Hu, and T. Zeng, "Improved secondary range compression focusing method in GEO SAR," *ICASSP*, 1373–1376, 2011.
31. Hu, C., Z. P. Liu, T. Zeng, et al., "An accurate imaging focusing method in GEO SAR," *ACTA Armamentarii*, Vol. 31, No. Suppl. 2, 28–32, 2010.
32. Davidson, G. W., I. G. Cumming, and M. R. Ito, "A chirp scaling approach for processing squint mode SAR data," *IEEE Transaction on Aerospace and Electronic Systems*, Vol. 32, No. 1, 121–133, 1996.
33. Raney, R. K., H. Runge, R. Bamler, et al., "Precision SAR processing using chirp scaling," *IEEE Trans. Geosci. Remote Sens.*, Vol. 32, No. 4, 786–799, Jul. 1994.
34. Moreira, A., J. Mittermayer, and R. Scheiber, "Extended chirp scaling algorithm for air- and spaceborne SAR data processing in stripmap and scan SAR imaging modes," *IEEE Trans. Geosci. Remote Sens.*, Vol. 34, No. 5, 1123–1136, Sep. 1996.
35. Carrara, W. G., R. S. Goodman, and R. M. Majewski, *Spotlight Synthetic Aperture Radar: Signal Processing Algorithms*, Artech House, Norwood, MA, 1995.
36. Bamler, R., "A comparison of range-doppler and wavenumber domain SAR focusing algoithms," *IEEE Trans. Geosci. Romote Sens.*, Vol. 30, No. 4, 706–713, 1992.
37. Cumming, I. G. and F. H. Wong, *Digital Processing of Synthetic Aperture Radar Data*, Artech House, 2005.
38. Carrara, W. G., R. S. Goodman, and R. M. Maiewski, *Spotlight Synthetic Aperture Radar: Signal Processing Algorithms*, Artech

House, Boston, 1995.

39. Wong, F. H. and T. S. Yeo, "New applications of nonlinear chirp scaling in SAR data processing," *IEEE Trans. Geosci. Remote Sens.*, Vol. 39, No. 5, 946–953, 2001.
40. Jin, M. J. and C. Wu, "A SAR correlation algorithm which accommodates large-range migration," *IEEE Trans. Geosci. Remote Sens.*, Vol. 22, No. 6, 592–597, 1984.
41. Neo, Y. L., F. Wong, and I. G. Cumming, "A two-dimensional spectrum for bistatic SAR processing using series reversion," *IEEE Geoscience and Remote Sensing Letters*, Vol. 4, No. 1, Jan. 2007.
42. Wong, F. H., I. G. Cumming, and Y. L. Neo, "Focusing bistatic SAR data using the nonlinear chirp scaling algorithm," *IEEE Trans. Geosci. Romote Sens.*, Vol. 46, No. 9, 2493–2505, Sep. 2008.